universe

MDPI

Article

Finite-Size Effects on the Critical End Point of Magnetized Quark Matter in the Nonlocal PNJL Model

G. Lugones [1,*], S. A. Ferraris [2] and A. G. Grunfeld [3,4]

[1] Centro de Ciências Naturais e Humanas, Universidade Federal do ABC, Avenida dos Estados 5001-Bangú, Santo André CEP 09210-580, SP, Brazil
[2] Physics Department, Comisión Nacional de Energía Atómica, Avenida del Libertador 8250, Ciudad Autónoma de Buenos Aires C1429BNP, Argentina; sebastianferraris18@gmail.com
[3] Consejo Nacional de Investigaciones Científicas y Técnicas, Godoy Cruz 2290, Ciudad Autónoma de Buenos Aires C1425FQB, Argentina; ag.grunfeld@conicet.gov.ar
[4] Instituto de Astronomía y Física del Espacio (IAFE, Consejo Nacional de Investigaciones Científicas y Técnicas-Universidad de Buenos Aires), Ciudad Universitaria, Ciudad Autónoma de Buenos Aires C1428EGA, Argentina
* Correspondence: german.lugones@ufabc.edu.br

Abstract

We investigate finite-size effects in the T–μ phase diagram of magnetized quark matter within the framework of a nonlocal extension of the Polyakov–Nambu–Jona-Lasinio (PNJL) model. Finite-size corrections are incorporated through the multiple reflection expansion (MRE) formalism, which describes a spherical quark droplet of radius R and modifies the density of states by including surface and curvature contributions. We consider two-flavor quark matter at finite temperature and chemical potential in the presence of a uniform magnetic field with strengths ranging from $eB = 0$ to 1 GeV^2, and droplet radii from $R = 3$ fm to the bulk limit. The nonlocal PNJL (nlPNJL) model naturally reproduces both magnetic catalysis at low temperatures and inverse magnetic catalysis near the chiral transition, in agreement with lattice QCD results. We analyze the chiral condensate, the traced Polyakov loop, the normalized quark condensate, and the corresponding susceptibilities. We find that finite-size effects do not modify the overall structure of the phase diagram, and that the coincidence of the chiral restoration and deconfinement transitions persists for all magnetic field strengths and system sizes explored, within the present implementation in which finite-size corrections are restricted to the fermionic sector. However, the critical end point (CEP) is notably shifted as a function of both magnetic field strength and system size: It moves toward higher chemical potentials and lower temperatures as system size decreases, an effect that is significantly amplified by strong magnetic fields. Our results have potential implications for the physics of phase conversion in compact stars and for the interpretation of relativistic heavy-ion collision experiments.

Keywords: effective models for quark matter; finite size effects; magnetized quark matter phase diagram

Check for updates

Academic Editors: Efrain J. Ferrer, Vivian de la Incera and Cristina Manuel

Received: 6 April 2026
Revised: 8 May 2026
Accepted: 16 May 2026
Published: 20 May 2026

Copyright: © 2026 by the authors. Licensee MDPI, Basel, Switzerland. This article is an open access article distributed under the terms and conditions of the Creative Commons Attribution (CC BY) license.

1. Introduction

Strong external magnetic fields comparable to or exceeding the QCD confining scale squared are expected to arise in several physical scenarios of current interest, making the study of their impact on the QCD phase diagram a subject of growing theoretical and phenomenological effort [1–3]. In compact astrophysical objects, the surface magnetic field of magnetars is estimated at $\sim 10^{15}$ G [4], and considerably higher values have been

conjectured for their deep interior, where some estimates suggest that the field strength could reach 10^{18}–10^{19} G if dense quark matter is present [5]. In relativistic heavy-ion collisions, transient magnetic fields are generated by the ultrarelativistic motion of the charged nuclei, reaching $eB \sim 10^{18}$–10^{19} G $\approx$ (0.005–0.05) GeV^2 at RHIC ($\sqrt{s} \sim 200$ GeV per nucleon) and $eB \sim 10^{19}$–10^{20} G $\approx$ (0.05–0.5) GeV^2 at the LHC [6]. Although short-lived ($\sim 10^{-23}$ s), these fields can affect the physics of the quark-gluon plasma, offering valuable opportunities to probe the phase diagram in the region of deconfinement and chiral symmetry restoration.

A common feature of the above scenarios is that the magnetized quark matter under consideration is not an infinite bulk system. In the interior of compact stars, a first-order deconfinement transition would proceed through the nucleation and growth of quark matter droplets, whose radii—ranging from a few to tens of femtometers—are set by the competition between bulk, surface, and curvature energy contributions [7]. Likewise, the quark-gluon plasma produced in heavy-ion collisions has a spatial extent of only a few femtometers, determined by the geometry of the colliding nuclei. Finite-size effects can modify the behavior of strongly interacting matter by restricting the available momentum space and suppressing long-wavelength fluctuations, potentially shifting the location of the CEP and altering the nature of the phase transition. Despite their potential phenomenological relevance, finite-size corrections have received comparatively less attention than magnetic-field effects in the literature on the QCD phase diagram. In this work, we address both effects simultaneously by studying the T–μ phase diagram of magnetized quark matter in a finite spherical geometry, within an effective model framework.

The nonperturbative character of strong interactions in this regime demands the use of either lattice QCD (LQCD) techniques or effective theories capable of capturing the essential features of QCD phenomenology. A prominent class of effective approaches is based on the Nambu–Jona-Lasinio (NJL) model [8,9], in which quarks interact through local four-point couplings that drive the spontaneous breakdown of chiral symmetry [10–12]. A significant improvement over the local formulation is achieved by introducing nonlocal separable interactions, a feature supported by several effective approaches to QCD and known to yield results in closer agreement with LQCD. For a detailed overview of nonlocal NJL models and their applications to strongly interacting matter under extreme conditions, see Ref. [13]. When supplemented with the coupling to a background temporal color gauge field through the Polyakov loop Φ [14], the resulting nlPNJL model [15–17] provides a simultaneous description of the chiral and deconfinement transitions whose pseudocritical temperatures are in good agreement with LQCD results [18].

A key feature of the QCD vacuum in the presence of an external magnetic field is the phenomenon of *magnetic catalysis* (MC): at zero temperature, the chiral condensate grows with the field strength, an effect that is well established both in LQCD and in essentially all effective models. Near the chiral crossover, however, LQCD simulations with physical quark masses [19,20] reveal a qualitatively different behavior: the condensate becomes a non-monotonic function of B and the pseudocritical temperature decreases with the field, an effect known as *inverse magnetic catalysis* (IMC). Reproducing IMC has proven challenging for most local effective models, which generically predict an increase of the transition temperature with the field [1–3]. Various remedies have been proposed, such as introducing explicit B-dependent couplings [21,22]. In contrast, nlPNJL models have been shown to account for IMC already at the mean-field level, without any field-dependent modification of the model parameters [23,24]. This natural emergence of IMC—rooted in the momentum dependence of the nonlocal quark self-energy—was demonstrated in the bulk limit at finite temperature T and zero chemical potential μ in Ref. [24], then at $T = 0$ and finite μ in Ref. [25], and subsequently extended to the full T–μ plane in Ref. [26]. These

bulk studies showed in particular that the CEP temperature decreases monotonically with eB, in sharp contrast to the predictions of local NJL/PNJL models [27–30], and that the chiral and deconfinement transitions remain overlapped throughout the T–μ–B parameter space.

In the past years, finite-volume effects in effective descriptions of strongly interacting matter have been investigated using several complementary approaches. Early studies within NJL-type models showed that the presence of compact spatial dimensions or boundaries modifies the pattern of chiral symmetry breaking and may affect the location and even the order of the chiral transition [31–33]. More recently, finite-volume effects have been analyzed in PNJL and related Polyakov-loop extended models, where the finite system size can affect both the chiral and deconfinement sectors through the quark contribution to the thermodynamic potential [34–37].

Different prescriptions have been employed to incorporate the finite spatial extent of the system. These include Monte Carlo simulations [34], functional-renormalization-group treatments that account for the restriction of long-wavelength fluctuations [38,39], compactification methods in which the spatial momenta are discretized according to the boundary conditions [33,40], and phenomenological implementations based on a lower momentum cutoff in the thermodynamic potential [35,37]. In addition, finite-size effects have been implemented through the Multiple Reflection Expansion (MRE) [41], which modifies the density of states by surface and curvature contributions and has been used to study thermodynamic quantities and the chiral/deconfinement crossover in finite PNJL systems [42]. Recent studies have further explored the dependence of the phase diagram and the CEP on the geometry, boundary conditions, and finite-volume prescription [43–45].

The present work builds on previous studies of the two-flavor nlPNJL model in the bulk, where strong-magnetic-field effects and the associated QCD phase structure were analyzed in Refs. [24–26]. We extend those results by incorporating, for the first time within this framework, finite-size corrections through the MRE formalism. The MRE describes a spherical quark droplet of radius R by modifying the density of states with surface and curvature contributions, thereby introducing an effective infrared cutoff that suppresses long-wavelength modes. This allows us to study the simultaneous interplay between magnetic-field effects, finite-size corrections, and the location of the CEP—a question that, to our knowledge, has not been addressed previously in the framework of nonlocal chiral quark models.

The article is organized as follows. In Section 2, we describe the theoretical formalism for magnetized quark matter within the nlPNJL model, including the MRE treatment of finite-size effects. In Section 3, we specify the model input and parameter choice, and discuss the infrared structure of the MRE density of states. In Section 4, we present our numerical results for the chiral and deconfinement order parameters and susceptibilities, considering different magnetic field strengths and system sizes. The resulting phase diagram in the T–μ plane is discussed in Section 5. Finally, in Section 6, we provide a summary and conclusions.

2. PNJL Formalism with Finite-Size and Magnetic-Field Effects

In this work, we consider the two-flavor nlPNJL model in the bulk, as developed in Refs. [24–26], and extend it by incorporating finite-size effects through the MRE. For completeness, we briefly review the bulk formalism to keep the presentation self-contained and to establish the baseline against which finite-size effects are assessed.

We consider quark matter composed of u and d quarks at finite temperature T and quark chemical potential μ, in the presence of a uniform and static external magnetic field $\boldsymbol{B} = B\,\hat{z}$. Confinement physics is modeled through the coupling to a homogeneous temporal background color field, encoded in the traced Polyakov loop Φ.

For clarity, we organize the discussion as follows. We first summarize the bulk mean-field thermodynamic potential in a magnetic background, then discuss its regularization and the main thermodynamic observables, and finally introduce the MRE treatment of finite-size effects for a spherical droplet.

2.1. Bulk Mean-Field Thermodynamic Potential

In the mean-field approximation (MFA), the regularized grand-canonical potential is built from the bulk nlPNJL thermodynamic potential in the presence of the magnetic field and the Polyakov-loop background; details of the calculation can be found in Refs. [24–26]. In the Polyakov gauge, one can take

$$\phi = \phi_3\,\lambda_3 + \phi_8\,\lambda_8\,, \tag{1}$$

with $\phi_8 = 0$ for the cases considered here, so that

$$\phi_r = -\phi_g = \phi_3\,, \qquad \phi_b = 0\,, \tag{2}$$

and the traced Polyakov loop becomes

$$\Phi = \frac{1}{3}\,\mathrm{Tr}\,e^{i\phi/T} = \frac{1+2\cos(\phi_3/T)}{3}\,. \tag{3}$$

The bulk MFA thermodynamic potential reads

$$\Omega^{\mathrm{MFA}}_{B,T,\mu} = \frac{\bar{\sigma}^2}{2G} - T\sum_{n=-\infty}^{\infty}\sum_{c=r,g,b}\sum_{f=u,d}\frac{|q_f B|}{2\pi}\int\frac{dp_3}{2\pi}\Bigg[\ln\Big(p_\parallel^2 + \big(M_{0,p_\parallel}^{\lambda_f,f}\big)^2\Big) + \sum_{k=1}^{\infty}\ln\Delta^f_{k,p_\parallel}\Bigg] + \mathcal{U}(\Phi,T)\,, \tag{4}$$

where

$$\Delta^f_{k,p_\parallel} = \Big(2k|q_f B| + p_\parallel^2 + M^{+,f}_{k,p_\parallel}M^{-,f}_{k,p_\parallel}\Big)^2 + p_\parallel^2\Big(M^{+,f}_{k,p_\parallel} - M^{-,f}_{k,p_\parallel}\Big)^2. \tag{5}$$

The momentum-dependent constituent masses are given by

$$M^{\lambda,f}_{k,p_\parallel} = (1-\delta_{k_\lambda,-1})\,m_c + \bar{\sigma}\,g^{\lambda,f}_{k,p_\parallel}\,, \tag{6}$$

with

$$g^{\lambda,f}_{k,p_\parallel} = \frac{4\pi}{|q_f B|}(-1)^{k_\lambda}\int\frac{d^2p_\perp}{(2\pi)^2}\,g(p_\perp^2+p_\parallel^2)\,e^{-p_\perp^2/B_f}L_{k_\lambda}\!\left(\frac{2p_\perp^2}{B_f}\right). \tag{7}$$

Here $L_n(x)$ denotes the Laguerre polynomial, $g(p^2)$ is the Fourier transform of the nonlocal form factor $\mathcal{G}(z)$ introduced in the model action, and we use the definitions

$$k_\pm = k - \frac{1}{2} \pm \frac{s_f}{2}\,, \qquad s_f = \mathrm{sign}(q_f B)\,, \qquad B_f = |q_f B|\,. \tag{8}$$

Moreover,

$$p_\parallel \equiv (p_3,\,\omega_n - i\mu + \phi_c) \qquad \Rightarrow \qquad p_\parallel^2 = p_3^2 + (\omega_n - i\mu + \phi_c)^2, \tag{9}$$

where $\omega_n = (2n+1)\pi T$ are the fermionic Matsubara frequencies. The external magnetic field $\boldsymbol{B}$ is taken to point along the 3-axis.

The Polyakov-loop effective potential is taken in the polynomial form of Refs. [46,47],

$$\frac{\mathcal{U}(\Phi,T)}{T^4} = -\frac{b_2(T)}{2}\Phi^2 - \frac{b_3}{3}\Phi^3 + \frac{b_4}{4}\Phi^4, \tag{10}$$

with

$$b_2(T) = a_0 + a_1\left(\frac{T_0}{T}\right) + a_2\left(\frac{T_0}{T}\right)^2 + a_3\left(\frac{T_0}{T}\right)^3. \tag{11}$$

As in Ref. [26], we use $a_0 = 6.75$, $a_1 = -1.95$, $a_2 = 2.625$, $a_3 = -7.44$, $b_3 = 0.75$, $b_4 = 7.5$, and $T_0 = 210\,\mathrm{MeV}$.

2.2. Regularization and Bulk Thermodynamic Observables

The momentum integral in Equation (4) is ultraviolet divergent. We regularize it by subtracting the corresponding free contribution and adding it back in a regularized form, namely

$$\Omega^{\mathrm{MFA,reg}}_{B,T,\mu} = \Omega^{\mathrm{MFA}}_{B,T,\mu} - \Omega^{\mathrm{free}}_{B,T,\mu} + \Omega^{\mathrm{free,reg}}_{B,T,\mu}. \tag{12}$$

Here, $\Omega^{\mathrm{free}}_{B,T,\mu}$ is obtained from Equation (4) by setting $\bar{\sigma} = 0$ while keeping the coupling to both the magnetic field and the Polyakov-loop background. The regularized free term can be written as

$$\Omega^{\mathrm{free,reg}}_{B,T,\mu} = \Omega_{\mathrm{mag}} + \Omega_{\mathrm{free\,gas}}, \tag{13}$$

where [48]

$$\Omega_{\mathrm{mag}} = -\frac{3}{2\pi^2}\sum_f (q_f B)^2\left[\zeta'(-1,x_f) + F(x_f)\right], \tag{14}$$

$$\Omega_{\mathrm{free\,gas}} = -T\sum_{c,f,k}\frac{|q_f B|}{2\pi}\alpha_k\int\frac{dp}{2\pi}\,G^f_{k,p}(\phi_c,\mu,T), \tag{15}$$

with

$$F(x_f) = \frac{x_f^2}{4} - \frac{1}{2}(x_f^2 - x_f)\ln x_f, \tag{16}$$

$$G^f_{k,p}(\phi_c,\mu,T) = \sum_{s=\pm}\ln\left[1 + \exp\left(-\frac{\epsilon^f_{kp} + i\phi_c + s\mu}{T}\right)\right]. \tag{17}$$

We have also defined

$$x_f = \frac{m_c^2}{2|q_f B|}, \qquad \alpha_k = 2 - \delta_{k0}, \qquad \epsilon^f_{kp} = \sqrt{p^2 + 2k|q_f B| + m_c^2}. \tag{18}$$

The mean fields $\bar{\sigma}(B,T,\mu)$ and $\Phi(B,T,\mu)$ are obtained from the stationarity conditions

$$\frac{\partial\Omega^{\mathrm{MFA,reg}}_{B,T,\mu}}{\partial\bar{\sigma}} = 0, \qquad \frac{\partial\Omega^{\mathrm{MFA,reg}}_{B,T,\mu}}{\partial\Phi} = 0. \tag{19}$$

Once the solution of these gap equations is found, other bulk observables follow in the standard way. In particular, the regularized quark condensate of flavor f is

$$\langle\bar{q}_f q_f\rangle^{\mathrm{reg}}_{B,T,\mu} = \frac{\partial\Omega^{\mathrm{MFA,reg}}_{B,T,\mu}}{\partial m_c}. \tag{20}$$

Here, we use the normalized flavor-averaged condensate, as in Ref. [24],

$$\bar{\Sigma}_{B,T} = \frac{1}{2}\left(\Sigma^u_{B,T} + \Sigma^d_{B,T}\right), \tag{21}$$

where

$$\Sigma^f_{B,T} = -\frac{2m_c}{S^4}\left[\langle\bar{q}_f q_f\rangle^{\rm reg}_{B,T,\mu} - \langle\bar{q}_f q_f\rangle^{\rm reg}_{0,0,0}\right], \tag{22}$$

and $S = (135 \times 86)^{1/2}$ MeV is a phenomenological scale.

The pseudocritical chiral and deconfinement temperatures are located from the maxima of the corresponding susceptibilities,

$$\chi_{\rm ch} = -\frac{\partial}{\partial T}\left[\frac{\langle\bar{u}u\rangle^{\rm reg}_{B,T,\mu} + \langle\bar{d}d\rangle^{\rm reg}_{B,T,\mu}}{2}\right], \qquad \chi_\Phi = \frac{\partial\Phi}{\partial T}. \tag{23}$$

With this definition, purely magnetic vacuum terms that do not depend on T do not contribute to $\chi_{\rm ch}$.

In the crossover regime, the location of the susceptibility peaks defines a *pseudocritical temperature* $T_{\rm pc}$. In the first-order regime, the transition temperature $T_{\rm tr}$ is instead identified by the degeneracy of the two minima of the thermodynamic potential. For brevity, where the distinction is not essential, we use the generic term "transition temperature" to refer to both cases.

2.3. Finite-Size Effects: MRE Description of a Spherical Droplet

To incorporate finite-size effects, we employ the MRE formalism for a spherical droplet of radius R [42,49]. In this approach the density of states is modified according to

$$\rho_{{\rm MRE},f}(p) = 1 + \frac{6\pi^2}{pR} f_{S,f}(p) + \frac{12\pi^2}{(pR)^2} f_{C,f}(p). \tag{24}$$

The surface contribution is

$$f_{S,f}(p) = -\frac{1}{8\pi}\left(1 - \frac{2}{\pi}\arctan\frac{p}{m_c}\right), \tag{25}$$

and for the curvature term we use the standard Madsen ansatz[1],

$$f_{C,f}(p) = \frac{1}{12\pi^2}\left[1 - \frac{3p}{2m_c}\left(\frac{\pi}{2} - \arctan\frac{p}{m_c}\right)\right]. \tag{26}$$

As emphasized in the MRE literature, $\rho_{{\rm MRE},f}(p)$ can become negative at sufficiently small momenta because higher-order terms in $1/R$ are neglected. To avoid this unphysical region, an infrared cutoff is introduced by requiring

$$\rho_{{\rm MRE},f}(p) = 0, \tag{27}$$

and taking $\Lambda_{\rm IR}$ as the largest root of this equation.

A few comments on the interpretation of this cutoff are in order. The suppression of long-wavelength modes is a physical finite-size effect: modes with wavelengths comparable to, or larger than, the droplet size do not fit inside the system and are therefore strongly affected by the boundary. The limitation of the MRE lies not in this infrared suppression itself, but in the fact that the MRE is a truncated semiclassical expansion in powers of $1/(pR)$. It is therefore quantitatively controlled for $pR \gg 1$, while for $p \lesssim 1/R$ higher-order terms become important. The negative density of states that appears at small momenta is a manifestation of this loss of control, and the infrared cutoff is a standard prescription used to exclude this unphysical region.

In the absence of a magnetic field, the replacement in a generic bulk momentum integral is

$$\frac{1}{(2\pi)^3}\int d^3p\ \cdots \longrightarrow \frac{1}{(2\pi)^3}\int_{\Lambda_{\rm IR}}^{\infty} 4\pi p^2\, dp\ \rho_{{\rm MRE},f}(p)\ \cdots . \tag{28}$$

In the presence of the magnetic field, the transverse motion is quantized into Landau levels and

$$p = \sqrt{p_3^2 + 2k|q_f B|}\,. \tag{29}$$

Hence, the relevant substitution in thermodynamic integrals becomes[2]

$$\frac{|q_f B|}{2\pi}\sum_{k=0}^{\infty}\alpha_k\int\frac{dp_3}{2\pi}\ \cdots \longrightarrow \frac{|q_f B|}{2\pi}\sum_{k=0}^{\infty}\alpha_k\int_{\Lambda_{\rm IR}}^{\infty}\frac{dp_3}{2\pi}\,\rho_{{\rm MRE},f}(p)\ \cdots , \tag{30}$$

where $\Lambda_{\rm IR}$ is the largest solution of $\rho_{{\rm MRE},f}(\sqrt{p_3^2 + 2k|q_f B|}) = 0$ with respect to p_3.

Within the present implementation, the MRE correction is applied only to the fermionic sector: the Polyakov-loop potential $\mathcal{U}(\Phi, T)$ is left unchanged and treated as a bulk gluonic effective potential. This choice is not merely a simplifying assumption; it follows the standard practice adopted in PNJL studies of finite-volume effects, where the Polyakov-loop potential is calibrated to pure-gauge lattice thermodynamics in the bulk and kept in that form when finite-size corrections are introduced in the fermionic sector through low-momentum cutoffs, MRE, or related prescriptions [35,36,42]. This procedure is supported on physical grounds by two complementary arguments.

First, as shown by Sasaki and Redlich [51], the effective olyakov-loop potential in SU(3) Yang–Mills theory can be derived from the partition function using the background field method, where the n-body gluon contributions are obtained by performing the integration over the color gauge group. The resulting potential is entirely determined by the group-theoretical structure of the Haar measure. Because $\mathcal{U}(\Phi, T)$ originates from this algebraic color integration rather than from a momentum-space integral over propagating modes, it is not subject to the modification of the density of states that the MRE formalism introduces: the surface and curvature corrections in Equation (24) have no counterpart in the group-integration procedure that generates $\mathcal{U}(\Phi, T)$.

Second, on dimensional grounds, the gluonic sector is governed by the confinement scale $\Lambda_{\rm QCD} \sim 200$–$300$ MeV, which corresponds to a correlation length $\xi_g \lesssim 1$ fm, well below the smallest droplet radius considered here ($R = 3$ fm). In contrast, quarks are affected more directly by the finite size of the system because their allowed momenta depend on the spatial extension of the droplet. It is therefore physically reasonable to expect that the leading finite-size corrections enter through the quark sector. We stress, however, that this is a plausibility argument rather than a derivation: a fully consistent treatment of finite-volume effects in the gluonic sector—which would require, for instance, a determination of the R-dependence of the parameters T_0, a_i, and b_i entering Equation (10)—lies beyond the scope of bulk-fitted PNJL-type effective potentials.

It is important to be explicit about the implications of this treatment for the interpretation of our results. Because $\mathcal{U}(\Phi, T)$ is calibrated in the bulk limit, it is not sensitive to the geometric suppression of infrared modes that the MRE imposes on the quark sector, and the R-dependence of Φ in our calculation arises indirectly through its coupling to the quark determinant. As a consequence, the coincidence of the chiral and deconfinement pseudocritical temperatures observed throughout this work—a result well established in the bulk limit [26]—should not be regarded as an independent prediction of the finite-volume dynamics of the gluonic sector, but rather as a feature of the present framework that survives the introduction of the fermionic finite-size corrections. A genuine assessment of

whether this coincidence persists in a fully finite-volume treatment of the pure-gauge sector would require a finite-size formulation of $\mathcal{U}(\Phi, T)$ itself, which is currently not available.

Having established the MRE replacement rules and the treatment of the Polyakov-loop potential, we can now write the finite-size corrected thermodynamic potential in a compact form. For this purpose, it is convenient to define the logarithmic kernel

$$\mathcal{F}^f_{k,p_\parallel} = \ln\left[\frac{p_\parallel^2 + m_c^2}{p_\parallel^2 + \left(M^{\lambda_f,f}_{0,p_\parallel}\right)^2}\right] + \sum_{k=1}^{\infty} \ln\left[\frac{\left(2k|q_f B| + p_\parallel^2 + m_c^2\right)^2}{\Delta^f_{k,p_\parallel}}\right], \tag{31}$$

which encodes the difference between the interacting and free quark contributions for each Landau level k and longitudinal momentum $p_\parallel$, as required by the regularization procedure of Equation (12). With this definition, the regularized finite-size thermodynamic potential takes the form

$$\begin{aligned}\Omega^{\mathrm{MRE}}_{\mathrm{reg}} = {} & \frac{\bar{\sigma}^2}{2G} + \mathcal{U}(\Phi, T) + \Omega_{\mathrm{mag}} + T \sum_{n,c,f} \frac{|q_f B|}{\pi} \int_{\Lambda_{\mathrm{IR}}}^{\infty} \frac{dp_3}{2\pi}\, \rho_{\mathrm{MRE},f}(p)\, \mathcal{F}^f_{k,p_\parallel} \\ & - T \sum_{c,f} \frac{|q_f B|}{2\pi} \sum_{k=0}^{\infty} \alpha_k \int_{\Lambda_{\mathrm{IR}}}^{\infty} \frac{dp_3}{2\pi}\, \rho_{\mathrm{MRE},f}(p)\, G^f_{k,p}(\phi_c, \mu, T).\end{aligned} \tag{32}$$

The first line contains the mean-field condensate energy, the Polyakov-loop potential, the magnetic vacuum contribution, and the MRE-corrected regularization of the quark determinant; the second line is the finite-size corrected free-gas contribution.

Finally, we remark that the model parameters entering the nonlocal form factor and the coupling constants are fixed in bulk vacuum,

$$T = 0\,, \qquad \mu = 0\,, \qquad eB = 0\,, \tag{33}$$

and then kept unchanged throughout the finite-T, finite-μ, finite-B, and finite-size analysis.

3. Model Input and Numerical Setup

In this section, we present the numerical results obtained from the formalism introduced above. Before discussing the behavior of the order parameters and the corresponding phase structure, it is necessary to specify the model input, namely the nonlocal form factor and the parameter sets used in the calculations.

3.1. Model Input and Parameter Choice

In order to obtain definite numerical predictions, one has to specify the functional form of the nonlocal form factor $g(p^2)$ appearing in Equation (7), together with the model parameters m_c, G, and Λ. In what follows, we adopt the Gaussian ansatz

$$g(p^2) = \exp\left(-p^2/\Lambda^2\right). \tag{34}$$

This choice is widely used in nonlocal chiral quark models and has the practical advantage that the integral entering Equation (7) can be carried out analytically, which considerably simplifies the subsequent numerical calculations. In addition, previous analyses within this class of models indicate that the qualitative features of the results are not expected to depend strongly on the specific shape of the form factor.

For the Gaussian form factor, the effective constituent quark masses introduced in Equation (6) take the form [24]

$$M_{k,p_\parallel}^{\pm,f} = (1-\delta_{k_\pm,-1})\, m_c + \bar{\sigma}\, \frac{\left(1-|q_f B|/\Lambda^2\right)^{k_\pm}}{\left(1+|q_f B|/\Lambda^2\right)^{k_\pm+1}} \exp\!\left(-p_\parallel^2/\Lambda^2\right). \tag{35}$$

Here Λ sets the effective soft momentum scale associated with the nonlocal interaction and therefore plays the role of an ultraviolet regulator in the model.

We fix the model parameters so as to reproduce physical observables at $\mu = B = 0$, adopting $-\langle\bar{q}q\rangle^{1/3} = 230\,\mathrm{MeV}$. This leads to $m_c = 6.4\,\mathrm{MeV}$, $\Lambda = 677.8\,\mathrm{MeV}$, and $G\Lambda^2 = 23.65$ [25], yielding $m_\pi = 139\,\mathrm{MeV}$ and $f_\pi = 92.4\,\mathrm{MeV}$.

Once a parameter set has been selected, the coupled gap equations, Equation (19), can be solved numerically for given values of the temperature T, chemical potential μ, and magnetic field B. As expected, for some regions of the (T,μ) plane and for a fixed magnetic field, more than one solution may coexist. In those cases, the physically realized state is identified with the solution that minimizes the corresponding thermodynamic potential.

The results presented below have been obtained following this prescription.

3.2. Infrared Cutoff in the MRE Density of States

Before presenting the thermodynamic results, it is worth discussing the infrared behavior of the MRE density of states in the presence of a magnetic field, since this feature is relevant for the numerical implementation of the formalism. In Figure 1, we show the quantity $p^2\rho_{\mathrm{MRE}}(p)$ for the lowest Landau level (LLL, $k=0$) and for several droplet radii, $R = 3$, 5, 10 fm, and the bulk limit. As discussed below, the infrared cutoff Λ_{IR} arises exclusively in the LLL; since the MRE density of states for $k=0$ does not depend on the magnetic field strength, the values of Λ_{IR} listed in Table 1 are determined solely by the droplet radius and the current quark mass, and remain unchanged for all values of eB considered in this work.

Table 1. Representative values of the infrared cutoff Λ_{IR} for light quarks as a function of the droplet radius R, using a common current mass $m_c = 6.5$ MeV for the u and d flavors. In the bulk limit, $R \to \infty$, one recovers $\Lambda_{\mathrm{IR}} = 0$.

R [fm]	Λ_{IR} [MeV]
3	52.53
5	33.54
10	18.88
∞	0

For finite-size droplets, the function $p^2\rho_{\mathrm{MRE}}(p)$ develops a zero in the low-momentum region and becomes negative below it. This is the well-known infrared pathology of the MRE approach, associated with the fact that the semiclassical density of states ceases to be reliable when surface corrections become too large compared with the bulk contribution. In order to exclude this unphysical region, one introduces an infrared cutoff Λ_{IR}, defined as the largest root of

$$p^2\rho_{\mathrm{MRE}}(p) = 0\,. \tag{36}$$

The momentum integrals are then restricted to the domain $p > \Lambda_{\mathrm{IR}}$, where the density of states remains positive.

As expected, the value of Λ_{IR} depends strongly on the droplet radius. Smaller systems lead to larger cutoff values, reflecting a stronger suppression of long-wavelength modes by finite-size effects. For the representative cases considered here, one finds $\Lambda_{\mathrm{IR}} \simeq 52.5$, 33.5, and 18.9 MeV for $R = 3$, 5, and 10 fm, respectively, while the cutoff moves close to the origin for $R = 100$ fm and vanishes in the bulk limit.

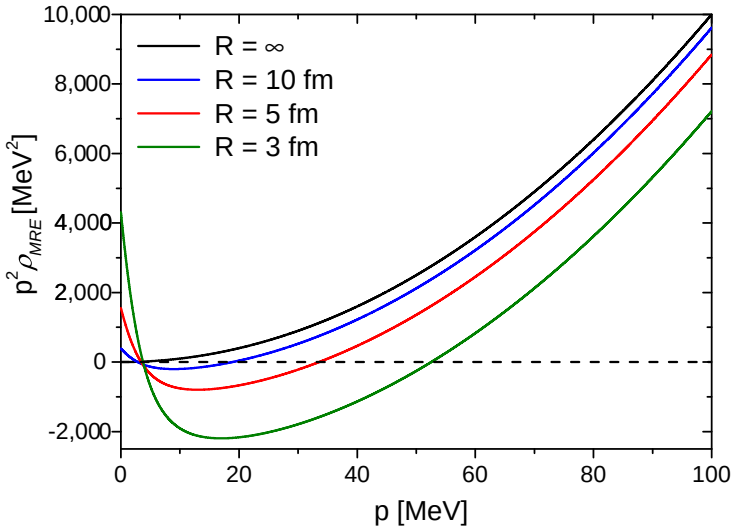


Figure 1. Behavior of $p^2\rho_{\mathrm{MRE}}(p)$ as a function of the momentum for the LLL and several droplet radii.

A distinctive feature of the present problem is that this infrared zero appears only in the LLL. For higher Landau levels ($k \geq 1$), the corresponding function $p^2\rho_{\mathrm{MRE}}(p)$ remains positive over the whole momentum range for all radii analyzed here, so that no infrared cutoff is required and one has $\Lambda_{\mathrm{IR}} = 0$. This special role of the LLL can be understood as a consequence of the effective dimensional reduction induced by the magnetic field: since the low-energy dynamics in the LLL is essentially restricted to the direction parallel to the field, boundary effects become comparatively more important, which enhances the sensitivity of this sector to finite-size corrections.

Therefore, the infrared cutoff introduced by the MRE formalism is not a generic feature of all Landau levels, but a specific finite-size effect of the LLL sector. This point is important for the discussion below, since it shows that the modification of the available phase space is highly selective and acts predominantly on the sector that dominates the low-energy dynamics in strong magnetic fields.

4. Order Parameters and Susceptibilities

In this section, we present the numerical results for the chiral and deconfinement order parameters as functions of temperature, for different values of the droplet radius R, the magnetic field strength eB, and the quark chemical potential μ. All figures in this section share a common panel layout: the left column displays finite-size effects at $eB = 0$ for several droplet radii ($R = \infty$, 10, 5, and 3 fm), while the right column shows the magnetic-field dependence in the bulk limit ($eB = 0$, 0.1, 0.5, and 1.0 GeV^2). Rows correspond to $\mu = 0$, 75, and 150 MeV (except for the susceptibilities, where only $\mu = 0$ and 75 MeV are shown). The bulk nlPNJL framework and some aspects of its thermodynamics were introduced in Refs. [24,26], where different parameter sets were considered. Here we restrict ourselves to a single representative parametrization but carry out a more detailed analysis of the bulk sector, presenting a systematic study of the chiral condensate, the Polyakov loop, the normalized quark condensate, and the corresponding susceptibilities as functions of temperature, chemical potential, and magnetic field strength. This extended bulk characterization serves both as a complement to the results of Refs. [24,26] and as the baseline against which finite-size effects are identified and quantified throughout this work.

4.1. Mean-Field $\bar{\sigma}$

We begin by analyzing the behavior of the mean-field $\bar{\sigma}$—the solution of the gap Equation (19)—as a function of temperature for different values of R, eB, and μ. The results are summarized in the six panels of Figure 2.

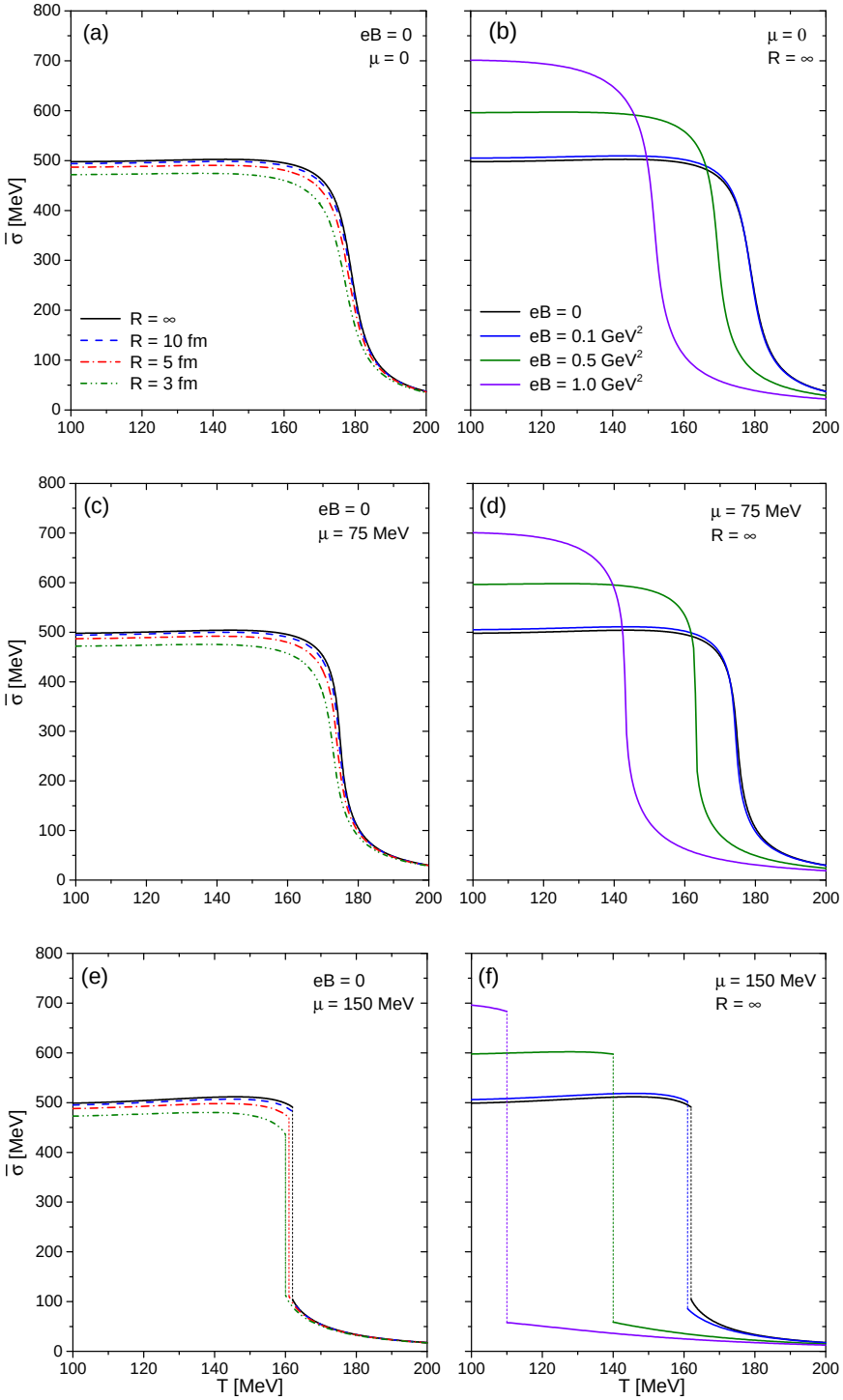


Figure 2. Mean-field $\bar{\sigma}$ as a function of the temperature T. **Left** column: finite-size effects at $eB = 0$ for several droplet radii. **Right** column: bulk limit ($R = \infty$) for different magnetic field strengths. Rows correspond to $\mu = 0$ [panels (**a**,**b**)], $\mu = 75$ MeV [panels (**c**,**d**)], and $\mu = 150$ MeV [panels (**e**,**f**)]. The left column illustrates the systematic shift of the crossover to lower temperatures with decreasing system size, while the right column displays the interplay between magnetic catalysis at low T and inverse magnetic catalysis near the pseudocritical temperature. At $\mu = 150$ MeV, the transition enters the first-order regime.

Three distinct mechanisms are found to modify the chiral transition: finite-size effects, the external magnetic field, and the quark chemical potential. We discuss each in turn, drawing on the figure panels for illustration.

Finite-size effects lower the chiral condensate at all temperatures and shift the crossover to lower temperatures, anticipating the partial restoration of chiral symmetry. At $\mu = 0$ and $eB = 0$ [panel (a)], the effect is modest for $R = 10$ fm but becomes clearly visible for $R = 3$ fm, where the vacuum value of $\bar{\sigma}$ is reduced by approximately 5% and the crossover shifts to noticeably lower T. Despite this shift, the transition remains a smooth crossover for all radii—no change in the order of the transition is induced purely by geometric confinement finite size effects. The same pattern persists at $\mu = 75$ MeV [panel (c)], where the crossover is steeper but the hierarchical ordering with R is preserved. At $\mu = 150$ MeV [panel (e)], the transition is already first order in the bulk and remains so for all radii; as in the previous cases, reducing R anticipates the partial restoration of chiral symmetry by shifting the transition to lower temperatures.

The magnetic field plays a dual role. At low temperatures, it enhances $\bar{\sigma}$ through *magnetic catalysis*: the quantization of transverse motion into Landau levels increases the degeneracy of low-energy states—particularly in the LLL, whose density of states grows linearly with $|q_f B|$—thereby strengthening the infrared dynamics that drive chiral symmetry breaking and leading to a larger value of the mean field $\bar{\sigma}$. This is clearly seen in the right column of Figure 2, where the low-T value of $\bar{\sigma}$ rises from $\sim$500 MeV at $eB = 0$ to $\sim$700 MeV at $eB = 1.0$ GeV^2. Near the transition, however, the behavior reverses: the pseudocritical temperature $T_{\rm pc}$ decreases monotonically with increasing eB—from $\sim$180 MeV at $eB = 0$ to $\sim$145 MeV at $eB = 1.0$ GeV^2 for $\mu = 0$ [panel (b)]—constituting the IMC effect. The competition between MC and IMC produces a characteristic crossing of the curves: for strong fields, $\bar{\sigma}(T)$ starts well above the $eB = 0$ curve but drops below it near $T_{\rm pc}$ [panels (b) and (d)]. It is remarkable that the nonlocal PNJL framework reproduces this behavior naturally [23,24], in agreement with lattice-QCD observations [19,20], without ad hoc modifications to the coupling constant or the Polyakov-loop potential. For moderate fields ($eB = 0.1$ GeV^2), the curves remain very close to the $eB = 0$ result, indicating that magnetic effects become phenomenologically significant only for $eB \gtrsim 0.1$ GeV^2.

A finite chemical potential steepens the crossover and lowers the transition temperature, pushing the system toward the first-order regime. At $\mu = 150$ MeV and strong magnetic fields [panel (f)], the transition is unambiguously first-order, with $\bar{\sigma}$ exhibiting a clear discontinuity and the low-temperature enhancement due to MC being even more pronounced than at lower μ.

These three effects act cumulatively: at a fixed point in the T–μ plane, reducing the system size, increasing the magnetic field, or raising the chemical potential can each push the system from the crossover regime into the first-order region, as the CEP shifts toward higher μ and lower T. It is important to note, however, that finite-size effects preserve the qualitative topology of the phase diagram: for all values of R and eB explored in this work, the transition remains a crossover at low chemical potentials and becomes first order at larger μ, with a CEP separating both regimes. What changes is the location of the CEP, not the overall structure of the phase diagram.

4.2. Deconfinement Order Parameter: The Polyakov Loop

Figure 3 displays the traced Polyakov loop Φ as a function of temperature, following the same panel layout as Figure 2.

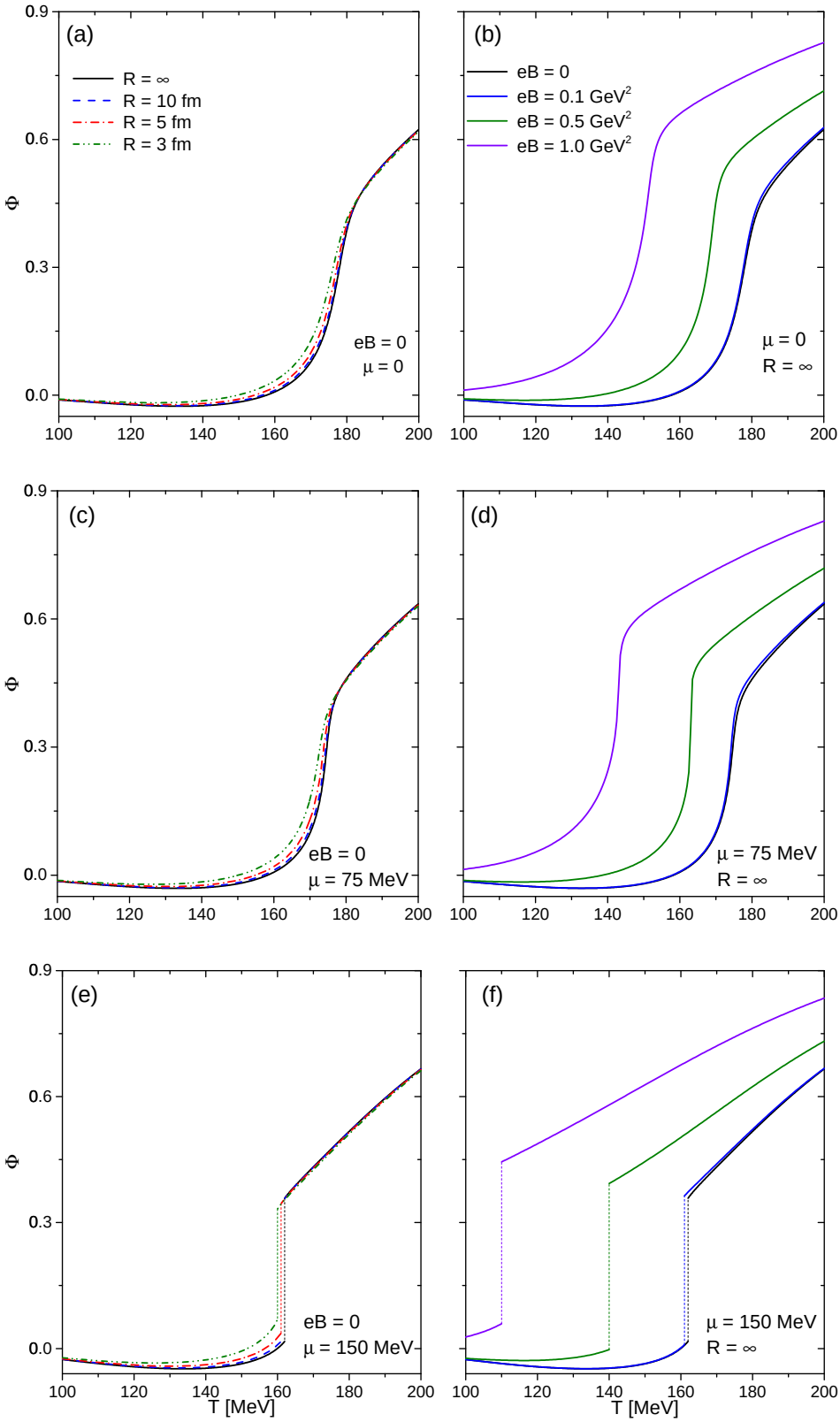


Figure 3. Traced Polyakov loop Φ as a function of the temperature T. **Left** column (**a**,**c**,**e**): finite-size effects at $eB = 0$ for several droplet radii. **Right** column (**b**,**d**,**f**): bulk limit for different magnetic field strengths. Rows correspond to different values of μ. The slightly negative values of Φ visible at low temperatures in some panels are an artifact of the polynomial parametrization of the Polyakov-loop potential (see discussion in the text). The pseudocritical temperature extracted from χ_Φ coincides with that obtained from $\chi_{\rm ch}$ for all values of R and eB considered (see Section 2 for discussion).

The behavior of Φ mirrors closely that of $\bar{\sigma}$: the three mechanisms identified in the preceding subsection—finite-size suppression, the dual role of the magnetic field, and the steepening induced by μ—manifest in the same way in the deconfinement sector. Reducing the droplet radius shifts the rise of Φ to lower temperatures [panels (a), (c), (e)], with the effect barely noticeable for $R = 10$ fm but clearly visible for $R = 3$ fm. In the bulk limit, increasing eB produces both an enhancement of the transition sharpness and a reduction of the pseudocritical temperature [panels (b), (d), (f)], consistently with the IMC effect. At $\mu = 150$ MeV and strong fields [panel (f)], Φ exhibits an abrupt jump, confirming the first-order character of the transition already identified through $\bar{\sigma}$.

A technical remark is in order: in some panels, Φ takes small negative values at the lowest temperatures. This is a known artifact of the polynomial parametrization of the Polyakov-loop potential, which does not enforce $\Phi \geq 0$ strictly, and has no consequence for the transition region. Likewise, the slight increase of Φ with eB at low T reflects the sensitivity of this quantity to the effective quark–gluon coupling in the model, and we refrain from attributing a direct physical meaning to this low-temperature behavior.

4.3. Normalized Flavor-Averaged Condensate $\bar{\Sigma}_{B,T}$

We also analyze the normalized flavor-averaged condensate $\bar{\Sigma}_{B,T}$ defined in Section 2, which is normalized to unity at $(T, eB) = (0, 0)$ and decreases toward zero as chiral symmetry is restored. Figure 4 presents $\bar{\Sigma}_{B,T}(T)$ following the same panel layout as in the preceding figures.

The behavior of $\bar{\Sigma}_{B,T}$ is fully consistent with the trends already identified for $\bar{\sigma}$ and Φ. Finite-size effects reduce the low-temperature plateau and shift the transition to lower T, with the suppression most visible for $R = 3$ fm [left column]. The magnetic field enhances $\bar{\Sigma}_{B,T}$ at low temperatures well above unity—reaching $\sim$1.5 at $eB = 0.5$ GeV^2 and $\sim$2.0 at $eB = 1.0$ GeV^2 for $\mu = 0$ [panel (b)]—providing a particularly clear manifestation of magnetic catalysis in a quantity directly comparable to lattice data. The pseudocritical temperature decreases with eB and the transition sharpens, becoming discontinuous at $\mu = 150$ MeV for $eB \geq 0.5$ GeV^2 [panel (f)].

The concordance among Figures 2–4 confirms the internal consistency of the calculation: finite-size suppression, IMC-driven reduction of $T_{\rm pc}$, and magnetic catalysis at low T manifest uniformly across the mean field, the Polyakov loop, and the normalized chiral condensate.

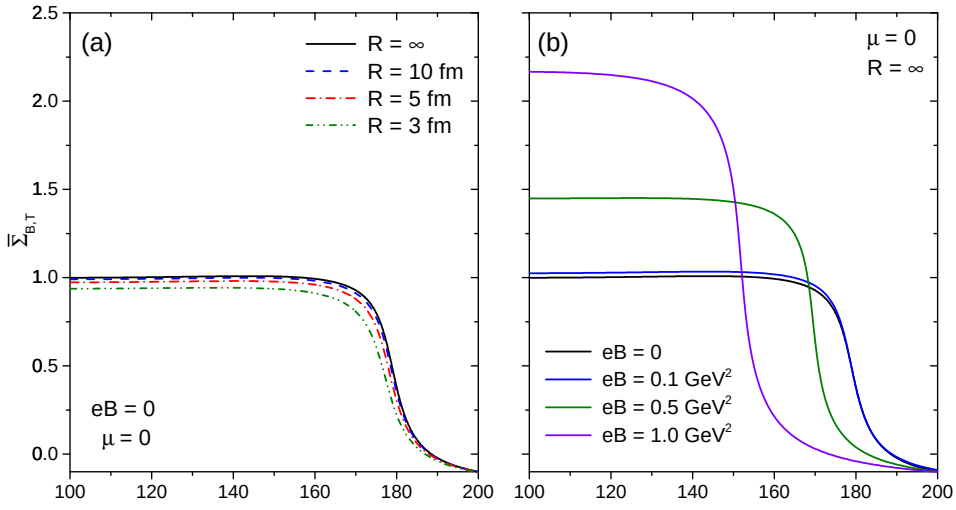


Figure 4. *Cont.*

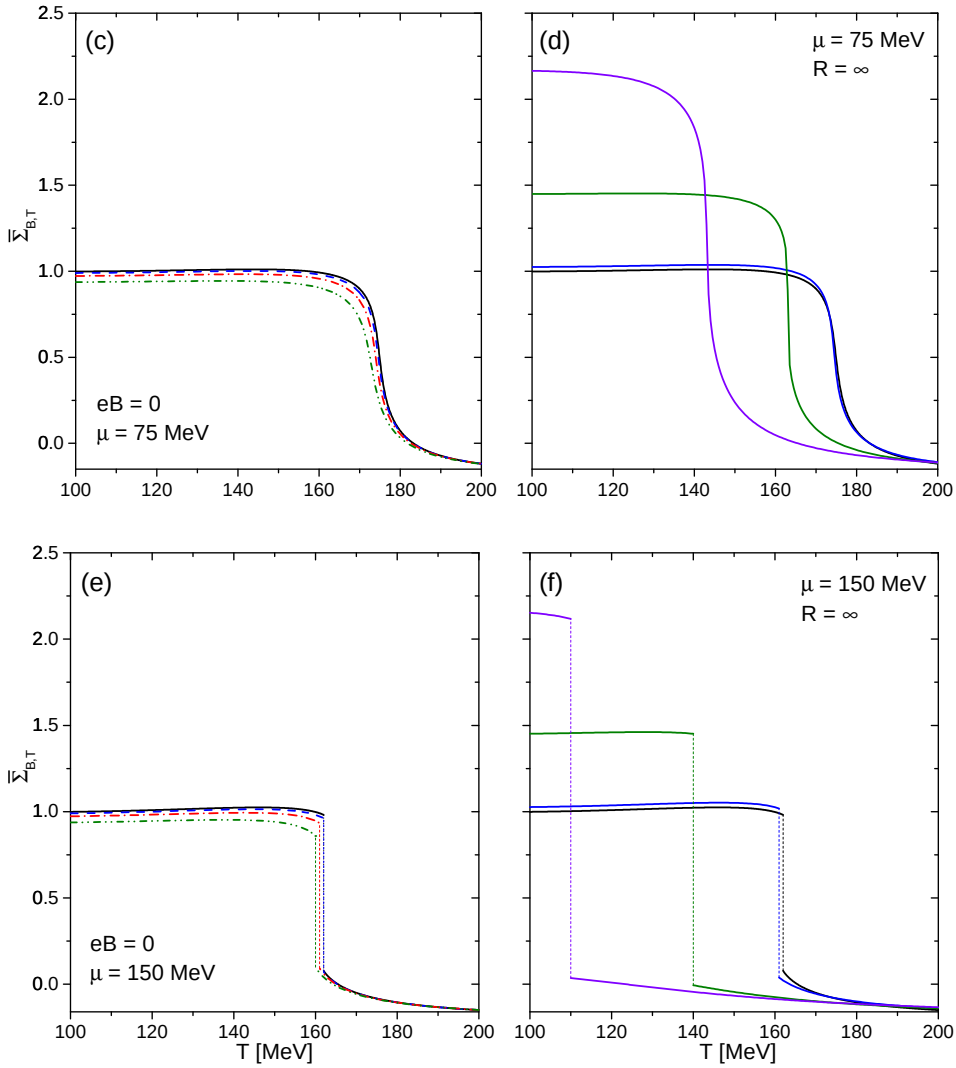


Figure 4. Normalized flavor-averaged condensate $\bar{\Sigma}_{B,T}$ as a function of the temperature T. **Left** column: finite-size effects at $eB = 0$ for several droplet radii ($R = \infty$, 10, 5, and 3 fm). **Right** column: bulk limit ($R = \infty$) for different magnetic field strengths ($eB = 0$, 0.1, 0.5, and 1.0 GeV^2). Rows correspond to $\mu = 0$ [panels (**a**,**b**)], $\mu = 75$ MeV [panels (**c**,**d**)], and $\mu = 150$ MeV [panels (**e**,**f**)]. The enhancement of $\bar{\Sigma}_{B,T}$ above unity at low T in the right column is a manifestation of magnetic catalysis.

4.4. Chiral and Deconfinement Susceptibilities

The pseudocritical temperatures discussed above are determined quantitatively from the peaks of $\chi_{\rm ch}$ and χ_Φ, defined in Equation (23). Figure 5 shows both susceptibilities as functions of T for $\mu = 0$ and 75 MeV.

In all panels, the peaks of $\chi_{\rm ch}$ and χ_Φ coincide within numerical accuracy, confirming the simultaneous character of the chiral and deconfinement transitions established in the preceding subsections. This coincidence should be interpreted within the scope of the present implementation, where finite-size corrections act directly on the fermionic sector, while $\mathcal{U}(\Phi, T)$ is kept in its bulk form. Consequently, the finite-R behavior of Φ is induced indirectly through its coupling to the quark sector, and the persistence of the coincident peaks should not be viewed as an independent test of finite-volume gluonic dynamics.

Reducing the droplet radius shifts the peaks to lower temperatures and slightly reduces their height [left column], reflecting the smoothing of the crossover by finite-size effects. Increasing eB in the bulk limit [right column] also shifts the peaks to lower T—providing a direct quantitative measure of IMC—while making them markedly taller and narrower, signaling the approach to first-order behavior. At $\mu = 75$ MeV, the peaks are roughly twice

as tall as at $\mu = 0$ ($\sim$0.4–0.5 vs. $\sim$0.2–0.25 MeV^{-1}), and the sharpening with eB is even more pronounced: at $eB = 1.0$ GeV^2 [panel (d)], the peak is very sharp, indicating proximity to the critical endpoint.

These susceptibilities provide the pseudocritical temperatures used to construct the crossover lines in the phase diagram presented in the next section.

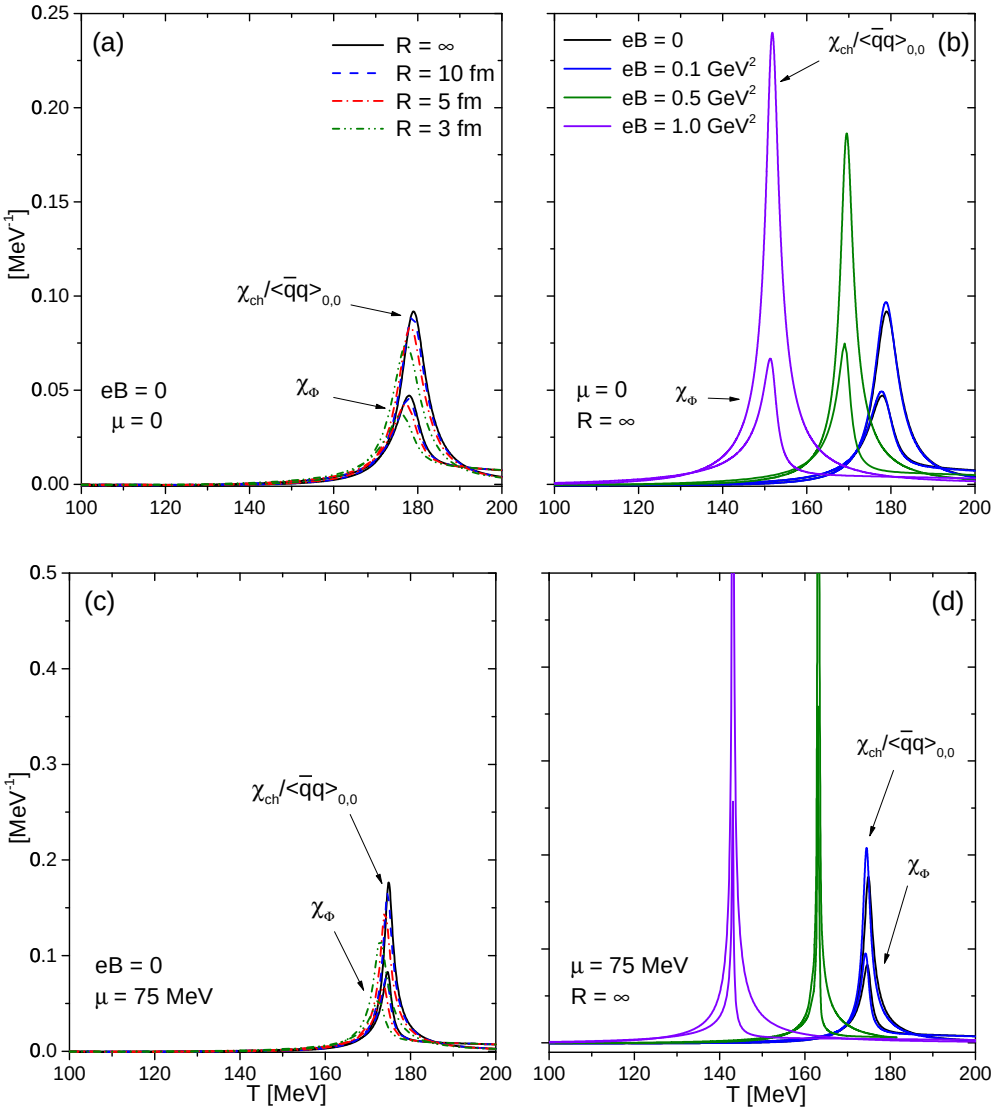


Figure 5. Chiral susceptibility $\chi_{\rm ch}/\langle\bar{q}q\rangle_{0,0}$ (solid curves) and Polyakov-loop susceptibility χ_Φ (dashed curves) as functions of the temperature T. **Left** column: finite-size effects at $eB = 0$ for several droplet radii ($R = \infty$, 10, 5, and 3 fm). **Right** column: bulk limit ($R = \infty$) for different magnetic field strengths ($eB = 0$, 0.1, 0.5, and 1.0 GeV^2). The upper row corresponds to $\mu = 0$ [panels (**a**,**b**)] and the lower row to $\mu = 75$ MeV [panels (**c**,**d**)]. The peaks of $\chi_{\rm ch}$ and χ_Φ coincide within numerical accuracy for all values of R and eB considered, with the caveats discussed in Section 2.

5. Phase Diagram in the T–μ Plane

We now assemble the information extracted from the order parameters and susceptibilities into the phase diagram in the T–μ plane. Given that the peaks of the chiral and Polyakov-loop susceptibilities occur at nearly the same temperature for all values of μ, eB, and R explored, we adopt the chiral susceptibility $\chi_{\rm ch}$ to define the pseudocritical crossover temperature. In the first-order regime, the transition temperature is identified by the Maxwell construction (equal depth of the two minima of the thermodynamic potential), and the CEP is located as the boundary between the crossover and first-order branches.

The resulting pseudocritical temperatures at $\mu = 0$ and CEP coordinates are collected in Tables 2 and 3, respectively.

Table 2. Pseudocritical temperature $T_{\rm pc}$ in MeV at zero chemical potential, for each combination of magnetic field strength eB and droplet radius R explored in this work.

	$R = \infty$	$R = 10$ fm	$R = 5$ fm	$R = 3$ fm
$eB = 0$	179.1	178.7	178.3	177.2
$eB = 0.1$ GeV^2	178.8	176.9	175.5	173.4
$eB = 0.5$ GeV^2	169.5	165.1	161.6	156.4
$eB = 1.0$ GeV^2	151.8	146.5	142.2	135.5

Table 3. Coordinates of the critical end point $(\mu_{\rm CEP}, T_{\rm CEP})$ in MeV, for all values of eB and R considered.

	$R = \infty$	$R = 10$ fm	$R = 5$ fm	$R = 3$ fm
$eB = 0$	(106, 171)	(107, 170)	(110, 169)	(118, 167)
$eB = 0.1$ GeV^2	(101, 171)	(109, 167)	(119, 164)	(134, 158)
$eB = 0.5$ GeV^2	(81, 162)	(99, 152)	(114, 141)	(130, 123)
$eB = 1.0$ GeV^2	(91, 139)	(106, 125)	(117, 112)	(126, 92)

Figure 6 presents the phase diagram for $eB = 0$, 0.1, 0.5, and 1.0 GeV^2, each panel showing curves for several droplet radii. In all cases, the phase structure consists of a first-order transition line (solid curves) meeting a crossover line (dashed curves) at a CEP (filled symbol), with the crossover corresponding simultaneously to partial chiral restoration and deconfinement.

The two main trends that emerge from the figure and the tables can be stated concisely. First, at fixed system size, increasing eB lowers the crossover temperature at low μ (inverse magnetic catalysis) while strengthening the first-order transition at higher densities. Table 2 shows that in the bulk limit $T_{\rm pc}(\mu = 0)$ drops from 179 MeV at $eB = 0$ to 152 MeV at $eB = 1.0$ GeV^2, a reduction of $\sim$27 MeV. The CEP temperature follows the same trend: $T_{\rm CEP}$ decreases from 171 MeV at $eB = 0$ to 139 MeV at $eB = 1.0$ GeV^2 in the bulk (Table 3). This monotonic decrease of $T_{\rm CEP}$ with the magnetic field is opposite to the behavior reported in most studies based on local NJL/PNJL models [27,28,30], and we attribute it to the natural emergence of IMC in the nonlocal framework as reported in Ref. [24] where it arises from the momentum dependence of the quark self-energy without ad hoc modifications.

Second, at fixed eB, decreasing the system size shifts the CEP toward higher μ and lower T—and the magnitude of this shift grows dramatically with the magnetic field. At $eB = 0$ [panel (a)], the effect is subtle: between $R = \infty$ and $R = 3$ fm the CEP moves by only $\sim$12 MeV in μ and $\sim$4 MeV in T, and the crossover curves for different radii are barely distinguishable except in the inset. At $eB = 0.1$ GeV^2 [panel (b)] the separation begins to grow, with the CEP for $R = 3$ fm already shifted to $(\mu, T) \approx (134, 158)$ MeV compared with $(101, 171)$ MeV in the bulk—a displacement of 33 MeV in μ and 13 MeV in T. At $eB = 0.5$ GeV^2 [panel (c)] the CEP positions for different radii are clearly resolved without magnification, and the spread reaches $\sim$49 MeV in μ and $\sim$39 MeV in T between the bulk and $R = 3$ fm. At $eB = 1.0$ GeV^2 [panel (d)] the finite-size effects are most dramatic: the $R = 3$ fm CEP lies at $(126, 92)$ MeV, some 35 MeV higher in μ and 47 MeV lower in T than the bulk value of $(91, 139)$ MeV. In this regime the phase diagrams for different radii differ qualitatively across the entire T–μ plane, not merely near the CEP.

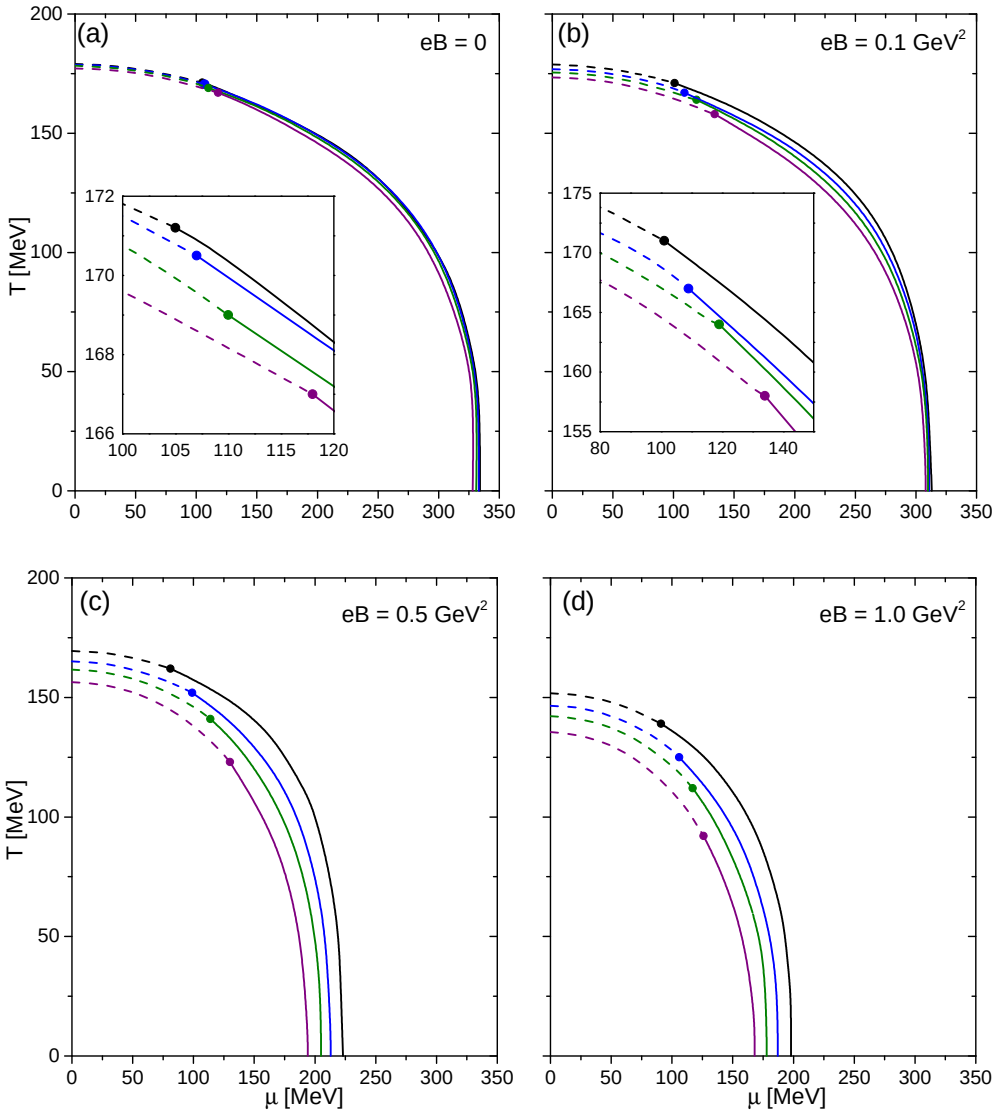


Figure 6. Phase diagram in the T–μ plane for different magnetic field strengths: $eB = 0$ [panel (**a**)], 0.1 GeV^2 [panel (**b**)], 0.5 GeV^2 [panel (**c**)], and 1.0 GeV^2 [panel (**d**)]. In each panel, solid lines denote the first-order transition and dashed lines denote the crossover, for several droplet radii: $R = \infty$ (black), 10 fm (blue), 5 fm (green), and 3 fm (violet). Filled symbols mark the location of the CEP. At $eB = 0$, the CEP coordinates are approximately $(\mu_{\rm CEP}, T_{\rm CEP}) = (105, 171)$ MeV for the bulk limit, $(107, 170)$ MeV for $R = 10$ fm, $(110, 169)$ MeV for $R = 5$ fm, and $(118, 167)$ MeV for $R = 3$ fm. Insets in panels (**a**,**b**) provide a magnified view of the CEP region.

This amplification of finite-size effects by the magnetic field can be understood from the interplay between Landau quantization and geometric confinement. The dimensional reduction associated with the lowest Landau level concentrates the low-energy dynamics along the field direction, enhancing the sensitivity to infrared physics. The MRE infrared cutoff $\Lambda_{\rm IR}$, which precisely suppresses long-wavelength modes in the LLL sector, therefore has a progressively larger impact on the phase structure as eB increases. The pseudocritical temperatures at $\mu = 0$ confirm this picture quantitatively: Table 2 shows that the spread in $T_{\rm pc}$ between $R = \infty$ and $R = 3$ fm increases from less than 2 MeV at $eB = 0$ to more than 16 MeV at $eB = 1.0$ GeV^2.

For $R = 3$ fm, one has $1/R \simeq 65$ MeV, while the corresponding MRE cutoff for light quarks is $\Lambda_{\rm IR} \simeq 52.5$ MeV. Thus, the cutoff acts precisely in the momentum region where the truncated expansion is least controlled. This does not invalidate the qualitative finite-size mechanism, but it implies that the corresponding numerical shift of the CEP should be

regarded as prescription-dependent. At $B = 0$, the infrared region affected by the cutoff is weighted by the three-dimensional phase-space measure p^2dp, which suppresses the relative contribution of the lowest momenta to the thermodynamic integrals. Therefore, the cutoff modifies the thermodynamics but does not dominate the full momentum integration. In a strong magnetic field, however, Landau-level quantization reduces the effective dimensionality of the low-energy phase space. In particular, when the lowest Landau level becomes dominant, the infrared modes removed by the cutoff carry comparatively more weight. This explains why the finite-size shift is amplified at large eB.

Therefore, the trends found in this work—the displacement of the CEP toward larger chemical potentials and lower temperatures with decreasing R, and the enhancement of this displacement by the magnetic field—are interpreted as robust consequences of geometric infrared suppression and Landau-level dimensional reduction. The precise numerical CEP coordinates, especially for the limiting case $R = 3$ fm at large eB, should instead be understood as model- and prescription-dependent.

These results indicate that finite-size corrections, which are often neglected in effective-model studies, can have a significant quantitative impact on the predicted location of the CEP—particularly in the presence of strong magnetic fields. This observation is relevant both to the interpretation of heavy-ion collision experiments, where the QGP has a spatial extent of a few femtometers, and to the microphysics of phase conversion in the interior of compact stars, where quark matter droplets could nucleate in the presence of intense magnetic fields.

6. Summary and Conclusions

We have studied the QCD phase diagram at finite temperature and chemical potential in the presence of an external, static, and uniform magnetic field, incorporating finite-size effects via the MRE formalism. Our analysis has been carried out in the framework of a two-flavor nlPNJL model, which has the distinctive feature of reproducing the IMC effect observed in lattice-QCD calculations without the need for ad hoc modifications to the model parameters.

The main results of this work can be summarized as follows:

(i) Previous studies in the bulk limit have shown that the nonlocal PNJL model naturally exhibits magnetic catalysis at low temperatures and inverse magnetic catalysis near the pseudocritical temperature [23,24,26]. In the present work, we demonstrate that these features remain robust in the presence of finite-size effects: for all system sizes considered and at finite chemical potential, the chiral condensate increases with the magnetic field at low temperatures, while the pseudocritical temperature $T_{\rm pc}$ decreases monotonically with eB.

(ii) The crossover transitions, characterized respectively by the chiral susceptibility $\chi_{\rm ch}$ and the Polyakov-loop susceptibility χ_Φ, occur simultaneously throughout the explored parameter space. This coincidence, already known in the bulk limit, is shown here to persist in magnetized quark matter after the inclusion of finite-size effects, down to $R = 3$ fm. Since the MRE corrections are applied only to the fermionic sector while $\mathcal{U}(\Phi, T)$ is kept in its bulk form—a standard choice in PNJL studies of finite-volume effects, supported by the hierarchy between the gluonic correlation length and the droplet radii considered here—the R-dependence of Φ is inherited from its coupling to the quarks, and a fully independent test of this coincidence at finite volume would require a finite-size formulation of the pure-gauge sector.

(iii) The qualitative structure of the phase diagram—consisting of a crossover region at low μ and a first-order transition line at higher μ, separated by a CEP—is maintained for all values of eB and R explored (see Table 3 for a complete listing of the CEP coordinates). In

the bulk limit, the CEP temperature decreases monotonically with the magnetic field, from $T_{\mathrm{CEP}} \simeq 171$ MeV at $eB = 0$ to $T_{\mathrm{CEP}} \simeq 140$ MeV at $eB = 1$ GeV^2, while the chemical potential μ_{CEP} remains in a relatively narrow range ($\sim$80–105 MeV). This behavior is opposite to that found in most studies based on local NJL/PNJL models [27–30,52], and we attribute this qualitative difference to the natural emergence of IMC in the nonlocal framework. Indeed, in local models, the behavior of T_{CEP} with the magnetic field is significantly modified when a B-dependent effective coupling is introduced to mimic IMC [30].

(iv) Finite-size effects shift the CEP toward higher chemical potentials and lower temperatures. At $eB = 0$, this shift is modest: from $(\mu_{\mathrm{CEP}}, T_{\mathrm{CEP}}) \approx (105, 171)$ MeV in the bulk to $(118, 167)$ MeV for $R = 3$ fm. However, the sensitivity of the phase structure to the system size is significantly amplified by the magnetic field. At $eB = 1$ GeV^2, the CEP positions for different radii are well separated across the entire T–μ plane, reflecting the interplay between the dimensional reduction induced by Landau quantization and the infrared mode suppression imposed by the MRE formalism.

The physical origin of this amplification can be understood as follows. In a strong magnetic field, the transverse quark motion is quantized into discrete Landau levels separated by gaps of order $|q_f B|$. As the field strength increases, the higher levels become energetically suppressed, and the low-energy dynamics are increasingly dominated by the LLL, in which only the longitudinal momentum component p_3 remains as a continuous degree of freedom. The system thus undergoes an effective dimensional reduction from three to one momentum-space dimension. In a bulk system ($R \to \infty$), this concentration of spectral weight in the LLL modifies the phase structure but preserves the full infrared spectrum along p_3. When the system is confined to a finite volume, the MRE formalism introduces an effective infrared cutoff Λ_{IR} that suppresses long-wavelength modes. In the absence of a magnetic field, this cutoff removes modes from a three-dimensional momentum space, where the affected states represent a small fraction of the total density of states, and the thermodynamic impact is correspondingly modest. In contrast, when the magnetic field is strong enough to enforce LLL dominance, the infrared cutoff acts on the single remaining continuous momentum direction, removing a proportionally much larger fraction of the states that govern the low-energy thermodynamics. It is this combination of dimensional reduction and infrared suppression that makes the phase structure—and in particular the CEP location—increasingly sensitive to the system size as eB grows.

It is important to distinguish which aspects of these results are expected to be robust and which may depend on the specific implementation of finite-size effects. The qualitative trends—namely, that confinement to a finite volume shifts the CEP toward higher μ and lower T, and that this shift is amplified by the magnetic field—rest on general physical grounds: the suppression of infrared modes by geometric confinement and the dimensional reduction induced by Landau quantization are well-established features that do not depend on the MRE formalism. The quantitative magnitude of the effect, however, is more sensitive to the details of the finite-size treatment. The MRE models the boundary as a sharp spherical surface with specific boundary conditions—an idealization of the actual diffuse interface—and, being a semiclassical expansion in powers of $1/R$, it may become less accurate at the smallest radii.

(v) Finite-size effects also modify the mean field and the chiral condensate: reducing the system radius suppresses the chiral condensate at temperatures below the transition and shifts the crossover to lower temperatures, smoothing the transition. At a fixed point in the T–μ plane, these effects act cumulatively with those of the magnetic field and the chemical potential: reducing R, increasing eB, or raising μ can each push the system from the crossover regime into the first-order region, as the CEP shifts accordingly. However, as

noted in point (iii), the overall topology of the phase diagram—crossover at low μ, first order at higher μ, separated by a CEP—is preserved for all parameter combinations explored.

Our analysis has been restricted to two flavors; however, the values of $\mu_{\rm CEP}$ obtained for all combinations of eB and R lie well below the strange quark threshold. In addition, Ref. [26] showed that IMC at finite μ is robust under moderate variations of the model parameters in the bulk limit. We therefore expect the qualitative trends reported here to survive the inclusion of strangeness, although a richer phase structure could appear at higher densities [52].

The findings of this work may have implications for relativistic heavy-ion collisions, where the quark-gluon plasma formed at the earliest stages is finite in size and exposed to intense, rapidly evolving magnetic fields. Since the magnitude and lifetime of these fields depend on the collision energy, centrality, and electromagnetic response of the medium, the lower and intermediate values of eB considered here provide the more conservative phenomenological range. By contrast, $eB = 1$ GeV^2 should be regarded as an extreme theoretical case, useful for probing the model's behavior rather than a quantitatively realistic heavy-ion scenario.

Within this interpretation, the large-field results show how Landau-level quantization, especially the increasing dominance of the lowest Landau level, amplifies the sensitivity of the CEP to finite-size infrared suppression. Therefore, the robust conclusion is not the precise numerical displacement of the CEP at $eB = 1$ GeV^2, but the qualitative trend that magnetic fields enhance finite-size effects in the phase diagram. This interplay between finite geometry and magnetic quantization provides a useful perspective for assessing how nonbulk effects may shape the QCD transition region in small, magnetized systems.

Author Contributions: Conceptualization, methodology, analysis, and writing, A.G.G. and G.L.; software and visualization, A.G.G. and S.A.F. All authors have read and agreed to the published version of the manuscript.

Funding: G.L. acknowledges the partial financial support from the Brazilian agency CNPq (grant 316844/2021-7). A.G.G. acknowledges the financial support from CONICET under Grant No. PIP 22-24 11220210100150CO and the National University of La Plata (Argentina), Project No. X960.

Data Availability Statement: The raw data supporting the conclusions of this article will be made available by the authors on request.

Conflicts of Interest: The authors declare no conflict of interest.

Abbreviations

The following abbreviations are used in this manuscript:

PNJL	Polyakov–Nambu–Jona-Lasinio
MRE	multiple reflection expansion
nlPNJL	non-local Polyakov–Nambu–Jona-Lasinio
CEP	critical endpoint
QCD	quantum chromodynamics
LQCD	lattice quantum chromodynamics
NJL	Nambu–Jona-Lasinio
MC	magnetic catalysis
IMC	inverse magnetic catalysis
MFA	mean field approximation
LLL	lowest Landau level

Notes

[1] The Madsen ansatz [50] for the curvature term smoothly interpolates between the massless MIT-bag limit, $f_C = -1/(24\pi^2)$, and the nonrelativistic Dirichlet limit, $f_C = 1/(12\pi^2)$, and was shown to reproduce shell-model calculations for massive quarks. A different choice of boundary condition would modify the numerical values of f_S and f_C but not the bulk Landau-level structure or the infrared mechanism discussed below, so the qualitative trends reported in this work are expected to be robust.

[2] It is worth stressing that the use of the MRE density of states in a magnetic field is a semiclassical prescription. The magnetic field is included through the Landau-level kinetic momentum (29) and the corresponding degeneracy factor, while the standard surface and curvature MRE functions are retained. A fully microscopic derivation of the spectral density in a finite magnetized domain could in principle generate additional terms depending on the magnetic length $\ell_B = 1/\sqrt{|q_f B|}$ and on the orientation of the boundary with respect to **B**. A systematic derivation and analysis of such anisotropic boundary corrections is beyond the scope and objectives of the present article.

References

1. Kharzeev, D.E.; Landsteiner, K.; Schmitt, A.; Yee, H.U. 'Strongly interacting matter in magnetic fields': An overview. In *Lecture Notes in Physics*; Springer: Berlin/Heidelberg, Germany, 2013; Volume 871, pp. 1–11. [CrossRef]
2. Andersen, J.O.; Naylor, W.R.; Tranberg, A. Phase diagram of QCD in a magnetic field: A review. *Rev. Mod. Phys.* **2016**, *88*, 025001. [CrossRef]
3. Miransky, V.A.; Shovkovy, I.A. Quantum field theory in a magnetic field: From quantum chromodynamics to graphene and Dirac semimetals. *Phys. Rep.* **2015**, *576*, 1–209. [CrossRef]
4. Duncan, R.C.; Thompson, C. Formation of very strongly magnetized neutron stars - implications for gamma-ray bursts. *Astrophys. J. Lett.* **1992**, *392*, L9. [CrossRef]
5. Chatterjee, D.; Elghozi, T.; Novak, J.; Oertel, M. Consistent neutron star models with magnetic field dependent equations of state. *Mon. Not. R. Astron. Soc.* **2015**, *447*, 3785. [CrossRef]
6. Skokov, V.; Illarionov, A.Y.; Toneev, V. Estimate of the magnetic field strength in heavy-ion collisions. *Int. J. Mod. Phys. A* **2009**, *24*, 5925–5932. [CrossRef]
7. Lugones, G. From quark drops to quark stars: Some aspects of the role of quark matter in compact stars. *Eur. Phys. J. A* **2016**, *52*, 53. [CrossRef]
8. Nambu, Y.; Jona-Lasinio, G. Dynamical Model of Elementary Particles Based on an Analogy with Superconductivity. 1. *Phys. Rev.* **1961**, *122*, 345–358. [CrossRef]
9. Nambu, Y.; Jona-Lasinio, G. Dynamical model of elementary particles based on an analogy with superconductivity. II. *Phys. Rev.* **1961**, *124*, 246–254. [CrossRef]
10. Vogl, U.; Weise, W. The Nambu and Jona Lasinio model: Its implications for hadrons and nuclei. *Prog. Part. Nucl. Phys.* **1991**, *27*, 195–272. [CrossRef]
11. Klevansky, S.P. The Nambu-Jona-Lasinio model of quantum chromodynamics. *Rev. Mod. Phys.* **1992**, *64*, 649–708. [CrossRef]
12. Hatsuda, T.; Kunihiro, T. QCD phenomenology based on a chiral effective Lagrangian. *Phys. Rep.* **1994**, *247*, 221–367. [CrossRef]
13. Dumm, D.G.; Carlomagno, J.P.; Scoccola, N.N. Strong-interaction matter under extreme conditions from chiral quark models with nonlocal separable interactions. *Symmetry* **2021**, *13*, 121. [CrossRef]
14. Fukushima, K. Chiral effective model with the Polyakov loop. *Phys. Lett. B* **2004**, *591*, 277–284. [CrossRef]
15. Contrera, G.A.; Gomez Dumm, D.; Scoccola, N.N. Nonlocal SU(3) chiral quark models at finite temperature: The Role of the Polyakov loop. *Phys. Lett. B* **2008**, *661*, 113–117. [CrossRef]
16. Hell, T.; Roessner, S.; Cristoforetti, M.; Weise, W. Dynamics and thermodynamics of a non-local PNJL model with running coupling. *Phys. Rev. D* **2009**, *79*, 014022. [CrossRef]
17. Carlomagno, J.P.; Gómez Dumm, D.; Scoccola, N.N. Deconfinement and chiral restoration in nonlocal SU(3) chiral quark models. *Phys. Rev. D* **2013**, *88*, 074034. [CrossRef]
18. Karsch, F.; Laermann, E. Thermodynamics and in medium hadron properties from lattice QCD. *Quark Gluon Plasma* **2003**, *3*, 1–59.
19. Bali, G.S.; Bruckmann, F.; Endrodi, G.; Fodor, Z.; Katz, S.D.; Krieg, S.; Schafer, A.; Szabo, K.K. The QCD phase diagram for external magnetic fields. *J. High Energy Phys.* **2012**, *2012*, 44. [CrossRef]
20. Bali, G.S.; Bruckmann, F.; Endrodi, G.; Fodor, Z.; Katz, S.D.; Schafer, A. QCD quark condensate in external magnetic fields. *Phys. Rev. D* **2012**, *86*, 071502. [CrossRef]
21. Farias, R.L.S.; Gomes, K.P.; Krein, G.I.; Pinto, M.B. Importance of asymptotic freedom for the pseudocritical temperature in magnetized quark matter. *Phys. Rev. C* **2014**, *90*, 025203. [CrossRef]
22. Ferreira, M.; Costa, P.; Lourenço, O.; Frederico, T.; Providência, C. Inverse magnetic catalysis in the (2+1)-flavor Nambu-Jona-Lasinio and Polyakov-Nambu-Jona-Lasinio models. *Phys. Rev. D* **2014**, *89*, 116011. [CrossRef]

23. Pagura, V.P.; Gomez Dumm, D.; Noguera, S.; Scoccola, N.N. Magnetic catalysis and inverse magnetic catalysis in nonlocal chiral quark models. *Phys. Rev. D* **2017**, *95*, 034013. [CrossRef]
24. Gómez Dumm, D.; Izzo Villafañe, M.F.; Noguera, S.; Pagura, V.P.; Scoccola, N.N. Strong magnetic fields in nonlocal chiral quark models. *Phys. Rev. D* **2017**, *96*, 114012. [CrossRef]
25. Ferraris, S.A.; Dumm, D.G.; Grunfeld, A.G.; Scoccola, N.N. Cold magnetized quark matter at finite density in a nonlocal chiral quark model. *Eur. Phys. J. A* **2021**, *57*, 141. [CrossRef]
26. Carlomagno, J.P.; Ferraris, S.A.; Gomez Dumm, D.; Grunfeld, A.G. T-μ quark matter phase transitions and critical endpoint in nonlocal PNJL models under a strong magnetic field. *Phys. Rev. D* **2023**, *108*, 056029. [CrossRef]
27. Avancini, S.S.; Menezes, D.P.; Pinto, M.B.; Providencia, C. The QCD Critical End Point Under Strong Magnetic Fields. *Phys. Rev. D* **2012**, *85*, 091901. [CrossRef]
28. Ferrari, G.N.; Garcia, A.F.; Pinto, M.B. Chiral Transition Within Effective Quark Models Under Magnetic Fields. *Phys. Rev. D* **2012**, *86*, 096005. [CrossRef]
29. Costa, P.; Ferreira, M.; Hansen, H.; Menezes, D.P.; Providência, C. Phase transition and critical end point driven by an external magnetic field in asymmetric quark matter. *Phys. Rev. D* **2014**, *89*, 056013. [CrossRef]
30. Costa, P.; Ferreira, M.; Menezes, D.P.; Moreira, J.; Providência, C. Influence of the inverse magnetic catalysis and the vector interaction in the location of the critical end point. *Phys. Rev. D* **2015**, *92*, 036012. [CrossRef]
31. Abreu, L.M.; Gomes, M.; da Silva, A.J. Chiral symmetry breaking in a finite volume. *Phys. Lett. B* **2006**, *642*, 551–562. [CrossRef]
32. Yasui, S.; Hosaka, A. Finite size effect on chiral symmetry breaking in the Nambu–Jona-Lasinio model. *Phys. Rev. D* **2006**, *74*, 054036. [CrossRef]
33. Abreu, L.M.; Malbouisson, A.P.C.; Malbouisson, J.M.C. Finite-size effects on the phase diagram of difermion condensates in two-dimensional four-fermion interaction models. *Phys. Rev. D* **2011**, *83*, 025001. [CrossRef]
34. Cristoforetti, M.; Hell, T.; Klein, B.; Weise, W. Finite-volume effects on phase transition in the Polyakov-loop extended Nambu–Jona-Lasinio model. *Phys. Rev. D* **2010**, *81*, 114017. [CrossRef]
35. Bhattacharyya, A.; Deb, P.; Ghosh, S.K.; Ray, R.; Sur, S. Thermodynamic Properties of Strongly Interacting Matter in Finite Volume using Polyakov-Nambu-Jona-Lasinio Model. *Phys. Rev. D* **2013**, *87*, 054009. [CrossRef]
36. Bhattacharyya, A.; Ray, R.; Sur, S. Fluctuation of strongly interacting matter in the Polyakov–Nambu–Jona-Lasinio model in a finite volume. *Phys. Rev. D* **2015**, *91*, 051501. [CrossRef]
37. Pan, Z.; Cui, Z.F.; Chang, C.H.; Zong, H.S. Finite-volume effects on phase transition in the Polyakov-loop extended Nambu–Jona-Lasinio model with a chiral chemical potential. *Int. J. Mod. Phys. A* **2017**, *32*, 1750067. [CrossRef]
38. Tripolt, R.A.; Braun, J.; Klein, B.; Schaefer, B.J. Effect of fluctuations on the QCD critical point in a finite volume. *Phys. Rev. D* **2014**, *90*, 054012. [CrossRef]
39. Braun, J.; Klein, B.; Schaefer, B.J. On the Phase Structure of QCD in a Finite Volume. *Phys. Lett. B* **2012**, *713*, 216–223. [CrossRef]
40. Abreu, L.M.; Corrêa, E.B.S.; Linhares, C.A.; Malbouisson, A.P.C. Finite-volume and magnetic effects on the phase structure of the three-flavor Nambu–Jona-Lasinio model. *Phys. Rev. D* **2019**, *99*, 076001. [CrossRef]
41. Balian, R.; Bloch, C. Distribution of eigenfrequencies for the wave equation in a finite domain. 1. Three-dimensional problem with smooth boundary surface. *Ann. Phys.* **1970**, *60*, 401–447. [CrossRef]
42. Grunfeld, A.G.; Lugones, G. Finite size effects in strongly interacting matter at zero chemical potential from Polyakov loop Nambu-Jona-Lasinio model in the light of lattice data. *Eur. Phys. J. C* **2018**, *78*, 640. [CrossRef]
43. Mata Carrizal, N.B.; Valbuena Ordóñez, E.; Garza Aguirre, A.J.; Betancourt Sotomayor, F.J.; Morones Ibarra, J.R. Effects of a Finite Volume in the Phase Structure of QCD. *Universe* **2022**, *8*, 264. [CrossRef]
44. Castaño-Yepes, J.D.; Paniagua, F.M.; Muñoz-Vitelly, V.; Ramirez-Gutierrez, C.F. Volume effects on the QCD critical end point from thermal fluctuations within the super statistics framework. *Phys. Rev. D* **2022**, *106*, 116019. [CrossRef]
45. Bernhardt, J.; Fischer, C.S.; Isserstedt, P.; Schaefer, B.J. Critical endpoint of QCD in a finite volume. *Phys. Rev. D* **2021**, *104*, 074035. [CrossRef]
46. Ratti, C.; Thaler, M.A.; Weise, W. Phases of QCD: Lattice thermodynamics and a field theoretical model. *Phys. Rev. D* **2006**, *73*, 014019. [CrossRef]
47. Schaefer, B.J.; Pawlowski, J.M.; Wambach, J. The Phase Structure of the Polyakov–Quark-Meson Model. *Phys. Rev. D* **2007**, *76*, 074023. [CrossRef]
48. Menezes, D.P.; Benghi Pinto, M.; Avancini, S.S.; Perez Martinez, A.; Providencia, C. Quark matter under strong magnetic fields in the Nambu-Jona-Lasinio Model. *Phys. Rev. C* **2009**, *79*, 035807. [CrossRef]
49. Grunfeld, A.G.; Izzo Villafañe, M.F.; Lugones, G. Surface and Curvature Tensions of Cold, Dense Quark Matter: A Term-by-Term Analysis Within the Nambu–Jona–Lasinio Model. *Universe* **2025**, *11*, 29. [CrossRef]
50. Madsen, J. Shell model versus liquid drop model for strangelets. *Phys. Rev. D* **1994**, *50*, 3328–3331. [CrossRef]

51. Sasaki, C.; Redlich, K. An Effective gluon potential and hybrid approach to Yang–Mills thermodynamics. *Phys. Rev. D* **2012**, *86*, 014007. [CrossRef]
52. Ferreira, M.; Costa, P.; Providência, C. Multiple critical endpoints in magnetized three flavor quark matter. *Phys. Rev. D* **2018**, *97*, 014014. [CrossRef]

Disclaimer/Publisher's Note: The statements, opinions and data contained in all publications are solely those of the individual author(s) and contributor(s) and not of MDPI and/or the editor(s). MDPI and/or the editor(s) disclaim responsibility for any injury to people or property resulting from any ideas, methods, instructions or products referred to in the content.